Journal of Computational Physics 349 (2017) 233–252

Contents lists available at ScienceDirect

Journal of Computational Physics

www.elsevier.com/locate/jcp

An efficient finite element method for simulation of droplet spreading on a topologically rough surface ☆

Li Luo [a,b], Xiao-Ping Wang [a,*], Xiao-Chuan Cai [c]

[a] Department of Mathematics, The Hong Kong University of Science and Technology, Hong Kong
[b] Shenzhen Institutes of Advanced Technology, Chinese Academy of Sciences, Shenzhen, 518055, PR China
[c] Department of Computer Science, University of Colorado Boulder, Boulder, CO 80309, USA

ARTICLE INFO

Article history:
Received 3 February 2017
Received in revised form 10 July 2017
Accepted 7 August 2017
Available online 31 August 2017

Keywords:
Wetting phenomenon
Topologically rough surface
Phase-field model
Unstructured finite element method
Mass compensation
Parallel computing

ABSTRACT

We study numerically the dynamics of a three-dimensional droplet spreading on a rough solid surface using a phase-field model consisting of the coupled Cahn–Hilliard and Navier–Stokes equations with a generalized Navier boundary condition (GNBC). An efficient finite element method on unstructured meshes is introduced to cope with the complex geometry of the solid surfaces. We extend the GNBC to surfaces with complex geometry by including its weak form along different normal and tangential directions in the finite element formulation. The semi-implicit time discretization scheme results in a decoupled system for the phase function, the velocity, and the pressure. In addition, a mass compensation algorithm is introduced to preserve the mass of the droplet. To efficiently solve the decoupled systems, we present a highly parallel solution strategy based on domain decomposition techniques. We validate the newly developed solution method through extensive numerical experiments, particularly for those phenomena that can not be achieved by two-dimensional simulations. On a surface with circular posts, we study how wettability of the rough surface depends on the geometry of the posts. The contact line motion for a droplet spreading over some periodic rough surfaces are also efficiently computed. Moreover, we study the spreading process of an impacting droplet on a microstructured surface, a qualitative agreement is achieved between the numerical and experimental results. The parallel performance suggests that the proposed solution algorithm is scalable with over 4,000 processors cores with tens of millions of unknowns.

1. Introduction

The study of the wetting phenomenon is of critical importance in many industrial applications such as coating, ink-jet printing, and microfluidics. Interesting wetting behavior occurs when micrometric spatial dimension comes into play, as a result roughness-enhanced wetting has become the subject of extensive investigation. When a droplet spreads on a topo-

☆ The research was supported in part by Chinese National 863 Plan Program under 2015AA01A302, NSFC Program 11501545, the NSFC-RGC joint research scheme N-HKUST620/15, and NSF DMS-1720366.

* Corresponding author.
E-mail addresses: lluoac@connect.ust.hk (L. Luo), mawang@ust.hk (X.-P. Wang), cai@cs.colorado.edu (X.-C. Cai).

http://dx.doi.org/10.1016/j.jcp.2017.08.010
0021-9991/

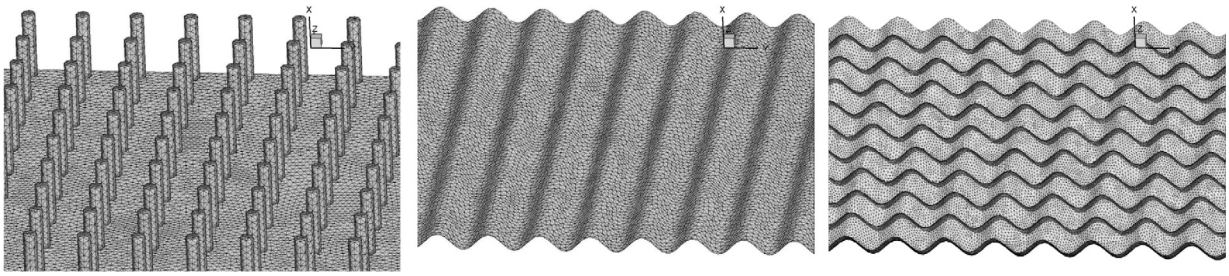

(a) circular posts (b) parallel strips (c) periodic waves

Fig. 1. Surfaces with various roughness.

logically rough surface with, for example, a pillar microstructure as illustrated in Fig. 1 (a), it may appear in two possible states: either the Wenzel state where the droplet infiltrates into the grooves and wets the bottom substrate between the posts, or the Cassie state where the droplet sits on top of the posts with pockets of air beneath it. The latter state results in a composite surface that exhibits superhydrophobic properties. The morphology of the liquid microstructures depends sensitively on the dimensions and spacing of the posts and may undergo a wetting transition between the Wenzel state and the Cassie state. Some authors have considered the conditions for the existence of different wetting regimes for sessile droplets, by means of analytic or numerical simulations based on the minimization of free energy [8,13,19,18,28,4,23]. In [18], the authors investigated the transition between the two states on a superhydrophobic surface by numerical simulations. They concluded that the equilibrium state of the droplet depends on the intrinsic contact angle and the position of the posts. Ren [23] used a string method to study the wetting transition on hydrophobic surfaces textured with a square lattice of pillars. The dependence of the energy barrier on the droplet size and the gap between the pillars was studied.

In systems involving three-dimensional droplets on rough surfaces, there are various contact angles along the contact line, and the droplets may assume a variety of shapes. Some applications require the knowledge of the contact angle as well as the contact angle hysteresis (CAH), i.e., the difference between maximum and minimum contact angles, which is generally attributed to surface heterogeneities and roughness. Lots of effort have been made to understand the effect of chemical heterogeneities on CAH for smooth surfaces, including striped patterns and regular chemical patches [2,14,18,29]. Studies for CAH on topologically rough surfaces were also attempted for some simplified model problems, such as the two-dimensional (or axisymmetric three-dimensional) problems of a droplet spreading on posts or sinusoidal surfaces [13,21,18,28]. These papers focused on the steady state prediction of the CAH, pinning of the contact line, and the existence of multiple local energy minima. Quasi-static results were obtained by increasing or decreasing the volume of the droplet.

In this paper, we study the CAH in dynamic cases by numerical simulation of a droplet spreading on a topologically rough surface. Different from the energy-based approaches in previous studies, the motion of the droplet and the surrounding air is described by a two-phase flow containing the liquid phase and the vapor phase. An issue in hydrodynamics with solid boundary is the incompatibility between the moving contact line and the no-slip boundary condition, as the latter leads to a non-integrable singularity, implying infinite viscous dissipation (see e.g. [20,7]). In [22], a phase field model consisting of the Cahn–Hilliard–Navier–Stokes equations with the GNBC is proposed to resolve the issue. This model has been used to simulate two-phase flows in two-dimensional channels with chemically patterns [27], as well as the dynamics of a three-dimensional droplet on smooth surface with chemical patches [10]. For the regular domains in these simulations, a finite difference scheme was used to discretize the governing equations on structured meshes. In the present work, we develop a new three-dimensional finite element solver on unstructured meshes and generalize the GNBC to arbitrarily complex surfaces. In order to construct a stable and efficient scheme for two-phase flows with large density and viscosity ratio, we combine a stabilized scheme [9] for the Cahn–Hilliard equation and a projection scheme [12,25] for the Navier–Stokes equations to fully decouple the phase function, the velocity, and the pressure. The GNBC is included in the weak form of the velocity system along different normal and tangential directions. Due to the truncation error, the total mass changes with small magnitude [5]. The accumulation of this effect usually causes the droplet to shrink and even to disappear [15,30]. To handle this issue, we apply a mass compensation algorithm to preserve both the total mass and the mass of the droplet by truncating and separately redistributing the phase field variable. For the three-dimensional simulations, the overall problem is computationally very demanding. To accelerate the convergence, we adopt a scalable domain decomposition method in which the computational mesh along with its associated data are distributed over many processors. We validate the newly developed solver through extensive numerical experiments on various rough surfaces (see Fig. 1). In particular, we study how wettability and droplet dynamics depend on the geometry and roughness of the surface.

The paper is organized as follows. In Section 2, the three-dimensional phase field model for two-phase flows is described. In Section 3, we recast the model into a variational form with a weak GNBC. The numerical scheme, the mass compensation algorithm, and the parallel solution strategy are demonstrated. In Section 4, numerical experiments of a droplet spreading on surfaces with various textures are presented. The paper is concluded in Section 5.

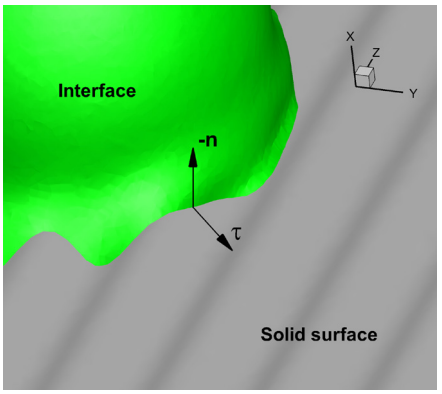

Fig. 2. The unit inward normal vector $-\mathbf{n}$ and unit tangential vector $\boldsymbol{\tau}$ at the liquid–solid interface.

2. The phase-field model

Let Ω be a bounded domain in $\mathbb{R}^3$, the two-fluids system can be described by a coupled Cahn–Hilliard and Navier–Stokes equations with the capillary force density, in the dimensionless form, as follows [10]:

$$\frac{\partial \phi}{\partial t} + \mathbf{u}\cdot\nabla\phi = \mathcal{L}_d \Delta\mu, \qquad \text{in} \quad \Omega, \tag{1}$$

$$\mu = -\epsilon\Delta\phi - \frac{\phi}{\epsilon} + \frac{\phi^3}{\epsilon}, \qquad \text{in} \quad \Omega, \tag{2}$$

$$Re\rho\left(\frac{\partial \mathbf{u}}{\partial t} + (\mathbf{u}\cdot\nabla)\mathbf{u}\right) = -\nabla p + \nabla\cdot(\eta D(\mathbf{u})) + \mathcal{B}\mu\nabla\phi + \mathbf{g}_{ext}, \qquad \text{in} \quad \Omega, \tag{3}$$

$$\nabla\cdot\mathbf{u} = 0, \qquad \text{in} \quad \Omega. \tag{4}$$

Here, a phase field variable ϕ is introduced to describe the transition between the two homogeneous equilibrium phases $\phi_\pm = \pm 1$. μ is the chemical potential, ϵ is the ratio between the interface thickness and the characteristic length, $\mu\nabla\phi$ is the capillary force. The mass density ρ and the dynamic viscosity η are interpolation functions of ϕ between fluid 1 and fluid 2, that is,

$$\rho = \frac{1+\phi}{2} + \lambda_\rho\frac{1-\phi}{2}, \qquad \eta = \frac{1+\phi}{2} + \lambda_\eta\frac{1-\phi}{2},$$

where $\lambda_\rho = \rho_2/\rho_1$ is the ratio of density between the two fluids and $\lambda_\eta = \eta_2/\eta_1$ is the ratio of viscosity. $\mathbf{u} = (u_x, u_y, u_z)$ where u_x, u_y, u_z are the velocity components along x, y, z directions, $D(\mathbf{u}) = \nabla\mathbf{u} + (\nabla\mathbf{u})^T$ is the rate of stress tensor, p is the pressure, $\mathcal{L}_d$ is the phenomenological mobility coefficient, Re is the Reynolds number and $\mathcal{B}$ measures the strength of the capillary force comparing to the Newtonian fluid stress (and $\mathcal{B}$ is inversely proportional to the capillary number). $\mathbf{g}_{ext} = (-Re\rho/Fr^2, 0, 0)$ where Fr is the Froude number.

The boundary $\partial\Omega$ consists of two parts, we denote them as the solid boundary Γ_w and the far field boundary $\partial\Omega\setminus\Gamma_w$. We denote $\mathbf{n}$ as the unit outward normal vector and $\boldsymbol{\tau}$ as the unit tangential vector of the surface, see Fig. 2.

The motion of the contact line that happens on the solid boundary can be described by a relaxation boundary condition for ϕ

$$\frac{\partial \phi}{\partial t} + \mathbf{u}_\tau\cdot\nabla_\tau\phi = -\mathcal{V}_s L(\phi), \qquad \text{on} \quad \Gamma_w, \tag{5}$$

and the GNBC for $\mathbf{u}$

$$\left((\mathcal{L}_s l_s)^{-1}\mathbf{u}_\tau - \mathcal{B}L(\phi)\nabla_\tau\phi/\eta + \mathbf{n}\cdot D(\mathbf{u})\right)\times\mathbf{n} = \mathbf{0}, \qquad \text{on} \quad \Gamma_w, \tag{6}$$

where $\mathcal{V}_s$ is a phenomenological parameter, $L(\phi) = \epsilon\partial_n\phi + \partial\gamma_{wf}(\phi)/\partial\phi$ measures the deviation of ϕ from equilibrium at the solid surface, and $\gamma_{wf}(\phi) = -\frac{\sqrt{2}}{3}\cos\theta_s^{surf}\sin(\frac{\pi}{2}\phi)$ is a function of the local composition measuring the fluid-solid interfacial free energy per unit area, where θ_s^{surf} is the static contact angle. $\mathcal{L}_s$ is the slip length of liquid, $l_s = \frac{1+\phi}{2} + \lambda_{l_s}\frac{1-\phi}{2}$ is an interpolation between two different wall-fluid slip lengths, and $\lambda_{l_s} = l_2/l_1$ is the ratio of slip length. $\mathbf{u}_\tau = \mathbf{u} - (\mathbf{n}\cdot\mathbf{u})\mathbf{n}$ is the boundary fluid velocity in the tangential direction. $\nabla_\tau = \nabla - (\mathbf{n}\cdot\nabla)\mathbf{n}$ is the gradient along the tangential direction. Equation (5) means that the material derivative of ϕ at the solid surface is proportional to the deviation from its equilibrium, and the minus sign ensures this evolution to be relaxational. Equation (6) governs the fluid slip at the solid surface.

In addition, a zero Neumann condition for μ

$$\partial_n \mu = 0, \qquad \text{on} \quad \Gamma_w, \tag{7}$$

and the following impermeability condition for $\mathbf{u}$

$$u_n := \mathbf{u}\cdot\mathbf{n} = 0, \qquad \text{on} \quad \Gamma_w, \tag{8}$$

are also imposed on the solid boundary.

On the far field boundary a stress-free outflow boundary condition is prescribed for the flow

$$-p + \eta\mathbf{n}\cdot D(\mathbf{u})\cdot\mathbf{n} = 0, \qquad \eta\mathbf{n}\cdot D(\mathbf{u})\cdot\boldsymbol{\tau} = 0, \qquad \text{on} \quad \partial\Omega\setminus\Gamma_w, \tag{9}$$

and zero Neumann conditions are prescribed for ϕ and μ

$$\partial_n\phi = 0, \qquad \partial_n\mu = 0, \qquad \text{on} \quad \partial\Omega\setminus\Gamma_w. \tag{10}$$

For initial conditions, in general, $\mu|_{t=0} = 0$, $p|_{t=0} = 0$, while $\phi|_{t=0}$ and $\mathbf{u}|_{t=0}$ are given differently for each experiment.

3. Numerical methods

3.1. A weak formulation

In this section, we derive a weak form of the governing equations (1)–(10) and show how the boundary conditions are incorporated in the weak form. We multiply (1) and (2) by a test function w, and then using integration by parts, the weak form of the Cahn–Hilliard equation is as follows: find $(\phi,\mu)\in H^1(\Omega)\times H^1(\Omega)$, such that for $\forall\ w\in H^1(\Omega)$,

$$\int_\Omega \frac{\partial\phi}{\partial t} w\mathrm{d}\Omega + \int_\Omega (\mathbf{u}\cdot\nabla)\phi w\mathrm{d}\Omega + \mathcal{L}_d\int_\Omega \nabla\mu\cdot\nabla w\mathrm{d}\Omega = \mathcal{L}_d\int_{\partial\Omega} w\partial_n\mu\mathrm{d}\Gamma, \tag{11}$$

and

$$\int_\Omega \mu w\mathrm{d}\Omega - \frac{1}{\epsilon}\int_\Omega(\phi^3-\phi)w\mathrm{d}\Omega - \epsilon\int_\Omega\nabla\phi\cdot\nabla w\mathrm{d}\Omega = -\epsilon\int_{\partial\Omega} w\partial_n\phi\mathrm{d}\Gamma. \tag{12}$$

Notice that from (7) and (10), we have

$$\mathcal{L}_d\int_{\partial\Omega} w\partial_n\mu\mathrm{d}\Gamma = 0, \quad \text{and} \quad \epsilon\int_{\partial\Omega\setminus\Gamma_w} w\partial_n\phi\mathrm{d}\Gamma = 0, \tag{13}$$

therefor, the boundary integrals of (12) can be reduced to the integrals on Γ_w. The relaxation boundary condition (5) can be included in (12) as:

$$\epsilon\int_{\Gamma_w} w\partial_n\phi\mathrm{d}\Gamma = -\int_{\Gamma_w} w\left(\frac{1}{\mathcal{V}_s}\left(\frac{\partial\phi}{\partial t} + \mathbf{u}_\tau\cdot\nabla_\tau\phi\right) + Q(\phi)\right)\mathrm{d}\Gamma, \tag{14}$$

where $Q(\phi) = -\frac{\sqrt{2}}{6}\pi\cos\theta_s^{surf}\cos\left(\frac{\pi}{2}\phi\right)$.

For the velocity field, we define space $\mathbf{V}(\Omega) := \left\{\mathbf{v}\in\mathbf{H}^1(\Omega):\ \mathbf{v}\cdot\mathbf{n}|_{\Gamma_w} = 0\right\}$ [24]. The weak form of the Navier–Stokes equations reads: find $(\mathbf{u},p)\in\mathbf{V}(\Omega)\times L^2(\Omega)$, such that for $\forall\ (\mathbf{v},q)\in\mathbf{V}(\Omega)\times L^2(\Omega)$,

$$\begin{aligned} &Re\int_\Omega \rho\left(\frac{\partial\mathbf{u}}{\partial t} + (\mathbf{u}\cdot\nabla)\mathbf{u}\right)\cdot\mathbf{v}\mathrm{d}\Omega - \mathcal{B}\int_\Omega \mu\nabla\phi\cdot\mathbf{v}\mathrm{d}\Omega - \int_\Omega \mathbf{g}_{ext}\cdot\mathbf{v}\mathrm{d}\Omega \\ &-\int_\Omega p\nabla\cdot\mathbf{v}\mathrm{d}\Omega + \int_\Omega \eta D(\mathbf{u})\cdot\nabla\mathbf{v}\mathrm{d}\Omega + \int_{\partial\Omega} p\mathbf{v}\cdot\mathbf{n} - \eta\mathbf{n}\cdot D(\mathbf{u})\cdot\mathbf{v}\mathrm{d}\Gamma = 0, \end{aligned} \tag{15}$$

and

$$\int_\Omega q\nabla\cdot\mathbf{u}\mathrm{d}\Omega = 0. \tag{16}$$

For the boundary integration, we define $\mathbf{v}_n := v_n\mathbf{n} = (\mathbf{v}\cdot\mathbf{n})\mathbf{n}$, $\mathbf{v}_\tau := v_\tau\boldsymbol{\tau} = (\mathbf{v}\cdot\boldsymbol{\tau})\boldsymbol{\tau}$, according to the identity $\mathbf{v} = \mathbf{v}_n + \mathbf{v}_\tau = v_n\mathbf{n} + v_\tau\boldsymbol{\tau}$,

$$\int_{\partial\Omega} p\mathbf{v}\cdot\mathbf{n} - \eta\mathbf{n}\cdot D(\mathbf{u})\cdot\mathbf{v}\mathrm{d}\Gamma = \int_{\partial\Omega} (p - \eta\mathbf{n}\cdot D(\mathbf{u})\cdot\mathbf{n})\, v_n \mathrm{d}\Gamma - \int_{\partial\Omega} \eta\mathbf{n}\cdot D(\mathbf{u})\cdot\boldsymbol{\tau}\, v_\tau \mathrm{d}\Gamma. \tag{17}$$

Since $\mathbf{v}\in\mathbf{V}(\Omega)$, $v_n = \mathbf{v}\cdot\mathbf{n} = 0$ on Γ_w, we have

$$\int_{\Gamma_w} (p - \eta\mathbf{n}\cdot D(\mathbf{u})\cdot\mathbf{n})\, v_n \mathrm{d}\Gamma = 0. \tag{18}$$

The GNBC for $\mathbf{u}$ on Γ_w can be included in the weak form as follows:

$$\begin{aligned} &-\int_{\Gamma_w} \eta\mathbf{n}\cdot D(\mathbf{u})\cdot\boldsymbol{\tau}\, v_\tau \mathrm{d}\Gamma \\ &= -\int_{\Gamma_w} \left(\mathcal{B}\left(\epsilon\partial_n\phi + Q(\phi)\right)\nabla_\tau\phi - \eta\left(\mathcal{L}_s l_s\right)^{-1}\mathbf{u}_\tau\right)\cdot\mathbf{v}_\tau \mathrm{d}\Gamma. \end{aligned} \tag{19}$$

On other boundaries $\partial\Omega\setminus\Gamma_w$, from (9), we have

$$\begin{aligned} &\int_{\partial\Omega\setminus\Gamma_w} p\mathbf{v}\cdot\mathbf{n} - \eta\mathbf{n}\cdot D(\mathbf{u})\cdot\mathbf{v}\mathrm{d}\Gamma \\ &= \int_{\partial\Omega\setminus\Gamma_w} (p - \eta\mathbf{n}\cdot D(\mathbf{u})\cdot\mathbf{n})\, v_n \mathrm{d}\Gamma - \int_{\partial\Omega\setminus\Gamma_w} \eta\mathbf{n}\cdot D(\mathbf{u})\cdot\boldsymbol{\tau}\, v_\tau \mathrm{d}\Gamma \\ &= 0. \end{aligned} \tag{20}$$

We remark that in the strong formulation of the problem the solid surface has to be smooth everywhere for the normal and tangents to be well defined, but in the weak formulation, because of the boundary treatment on Γ_w, we allow the solid surface to have some points for which the normal and tangents are not defined as long as the collection of these points has measure zero on the surface.

3.2. A semi-implicit finite element scheme

In order to construct a stable and efficient solver for the case of large density and viscosity ratio, we combine the idea of convex-splitting [9] for the Cahn–Hilliard equation and the pressure stabilization formulation [12] for the Navier–Stokes equations to fully decouple ϕ, $\mathbf{u}$, and p. The resulting decoupled systems are discretized by a finite element method in space.

Let Ω_h be a conforming tetrahedral mesh of Ω, and Γ_w^h is the solid boundary of Ω_h, denote by $(\cdot,\cdot)$ the $L^2(\Omega_h)$-inner product and by $\langle\cdot,\cdot\rangle_{\Gamma_w^h}$ the $L^2(\Gamma_w^h)$-inner product. We introduce three piecewise linear continuous finite element spaces $W_h\subset H^1(\Omega_h)$, $\mathbf{V}_h\subset\mathbf{V}(\Omega_h)$, and $W_h^0 = \left\{w_h\in W_h,\, w_h|_{\partial\Omega_h\setminus\Gamma_w^h} = 0\right\}$. Next, we introduce a time step length $\delta t > 0$. The scheme begins with a standard initialization step, i.e. ϕ_h^0, μ_h^0, $\mathbf{u}_h^0$, $p_h^0 (= p_h^{-1})$ are the finite element interpolations of $\phi|_{t=0}$, $\mu|_{t=0}$, $\mathbf{u}|_{t=0}$, $p|_{t=0}$, respectively, and

$$(\rho_h^0, \eta_h^0, l_{sh}^0) = \frac{1+\phi_h^0}{2} + (\lambda_\rho, \lambda_\eta, \lambda_{l_s})\frac{1-\phi_h^0}{2}.$$

Then, for $n\geq 0$, we proceed as follows:

Step 1: Solve the Cahn–Hilliard equation using a convex-splitting method: find $(\phi_h^{n+1}, \mu_h^{n+1})\in W_h\times W_h$, such that for $\forall\ w_h\in W_h$,

$$\left(\frac{\phi_h^{n+1}-\phi_h^n}{\delta t}, w_h\right) + (\mathbf{u}_h^n\cdot\nabla\phi_h^n, w_h) = -\mathcal{L}_d(\nabla\mu_h^{n+1}, \nabla w_h), \tag{21}$$

$$\begin{aligned} (\mu_h^{n+1}, w_h) = {}& \epsilon(\nabla\phi_h^{n+1}, \nabla w_h) + \frac{s}{\epsilon}(\phi_h^{n+1}, w_h) + \frac{1}{\epsilon}\left((\phi_h^n)^3 - (1+s)\phi_h^n, w_h\right) \\ &+ \left\langle\left(\frac{1}{\mathcal{V}_s}\left(\frac{\phi_h^{n+1}-\phi_h^n}{\delta t} + \mathbf{u}_{\tau,h}^n\cdot\nabla_\tau\phi_h^n\right)\right), w_h\right\rangle_{\Gamma_w^h} \\ &+ \left\langle Q\left(\phi_h^n\right) + \tilde{\alpha}(\phi_h^{n+1}-\phi_h^n), w_h\right\rangle_{\Gamma_w^h}. \end{aligned} \tag{22}$$

Step 2: Update ρ_h^{n+1}, η_h^{n+1} and $l_{s_h}^{n+1} \in W_h$:

$$(\rho_h^{n+1}, \eta_h^{n+1}, l_{s_h}^{n+1}) = \frac{1+\phi_h^{n+1}}{2} + (\lambda_\rho, \lambda_\eta, \lambda_{l_s})\frac{1-\phi_h^{n+1}}{2}. \tag{23}$$

Step 3: Solve the velocity system of Navier–Stokes equations using a pressure stabilization scheme: find $\mathbf{u}_h^{n+1} \in \mathbf{V}_h$, such that for $\forall\ \mathbf{v}_h \in \mathbf{V}_h$,

$$\begin{aligned}
&Re\left(\frac{\frac{1}{2}(\rho_h^{n+1}+\rho_h^n)\mathbf{u}_h^{n+1}-\rho_h^n\mathbf{u}_h^n}{\delta t}, \mathbf{v}_h\right)\\
&+Re\left(\left(\rho_h^{n+1}(\mathbf{u}_h^n\cdot\nabla)\mathbf{u}_h^{n+1}+\frac{1}{2}\left(\nabla\cdot(\rho_h^{n+1}\mathbf{u}_h^n)\right)\mathbf{u}_h^{n+1}\right), \mathbf{v}_h\right)\\
=&-\left(\eta_h^{n+1}\left(\nabla\mathbf{u}_h^{n+1}+(\nabla\mathbf{u}_h^{n+1})^T\right), \nabla\mathbf{v}_h\right)+\mathcal{B}(\mu_h^{n+1}\nabla\phi_h^{n+1}, \mathbf{v}_h)\\
&+(\mathbf{g}_{ext}, \mathbf{v}_h)-(2\nabla p_h^n-\nabla p_h^{n-1}, \mathbf{v}_h)-\left\langle\eta_h^{n+1}\left(\mathcal{L}_s l_{s_h}^{n+1}\right)^{-1}\mathbf{u}_{\tau,h}^{n+1}, \mathbf{v}_{\tau,h}\right\rangle_{\Gamma_w^h}\\
&+\mathcal{B}\left\langle\left(\epsilon\partial_n\phi_h^{n+1}+Q\left(\phi_h^{n+1}\right)+\tilde{\alpha}(\phi_h^{n+1}-\phi_h^n)\right)\nabla_\tau\phi_h^{n+1}, \mathbf{v}_{\tau,h}\right\rangle_{\Gamma_w^h}.
\end{aligned} \tag{24}$$

Step 4: Solve the pressure system of Navier–Stokes equations: find $p_h^{n+1} \in W_h$ satisfying $p_h^{n+1} = \eta_h^{n+1}\mathbf{n}\cdot D(\mathbf{u}_h^{n+1})\cdot\mathbf{n}$ on $\partial\Omega_h \setminus \Gamma_w^h$, such that for $\forall\ q_h \in W_h^0$,

$$\left(\nabla(p_h^{n+1}-p_h^n), \nabla q_h\right) = -\frac{\bar{\rho}}{\delta t}Re(\nabla\cdot\mathbf{u}_h^{n+1}, q_h), \tag{25}$$

where $\mathbf{v}_{\tau,h} = \mathbf{v}_h - (\mathbf{n}\cdot\mathbf{v}_h)\mathbf{n}$ and $\bar{\rho} = \min(1, \lambda_\rho)$. Under certain conditions for the choice of the two stabilization parameters s and $\tilde{\alpha}$, the scheme has the total energy decaying property and is stable. We refer to [10] for the stability analysis of the scheme.

Remark 3.1. The time discretization scheme constructed above leads to a decoupled system for the phase field variables, the velocity, and the pressure. At each time step, we solve a convection–diffusion equation for $\mathbf{u}$, a system of convection–diffusion/elliptic equations for (ϕ, μ), and a Poisson equation for p.

Remark 3.2. The particular way to discretize the quantity $Re\rho\left(\frac{\partial\mathbf{u}}{\partial t}+(\mathbf{u}\cdot\nabla)\mathbf{u}\right)$ by

$$Re\frac{\frac{1}{2}(\rho_h^{n+1}+\rho_h^n)\mathbf{u}_h^{n+1}-\rho_h^n\mathbf{u}_h^n}{\delta t}+Re\left(\rho_h^{n+1}(\mathbf{u}_h^n\cdot\nabla)\mathbf{u}_h^{n+1}+\frac{1}{2}\left(\nabla\cdot(\rho_h^{n+1}\mathbf{u}_h^n)\right)\mathbf{u}_h^{n+1}\right)$$

is to further decouple the mass conservation and the momentum conservation equations. We refer to [12] for the details.

3.3. A mass compensation algorithm

Notice that in Step 2 of the scheme, the variable density ρ_h^{n+1} and the dynamic viscosity η_h^{n+1} are interpolated using ϕ_h^{n+1}. The numerical values for ϕ_h^{n+1} may exceed the range $[-1, 1]$ in the case when the density ratio and viscosity ratio are large, leading to negative values of ρ_h^{n+1} and η_h^{n+1}. This issue was resolved by Chiu and Lin [5] by truncating and redistributing ϕ_h^{n+1} in order to preserve the total mass. However, because the interface has a small but finite thickness, shrinking of droplet occurs when ϕ_h^{n+1} shifts from its expected values in the bulk phases [15,30]. The situation is even worse in three dimensions since the volume of the droplet is usually less than 10% of the computational domain. Theoretical analysis in [30] suggests that there exists a critical radius r_c below which droplets will eventually disappear:

$$r_c = \left(\frac{2^{\frac{1}{6}}}{3\pi}V\epsilon\right)^{\frac{1}{4}},$$

where V is the volume of the whole computational domain Ω. To handle this issue, we propose a new algorithm based on an iterative redistribution process, as in Algorithm 1.

The idea of this algorithm is to compensate the lost mass of the liquid phase and to maintain the total mass unchanged so that both of the two phases retain their original mass. Specifically, after obtaining the updated ϕ_h^{n+1} from Step 1, we truncate the undershoot/overshoot values of ϕ_h^{n+1}, compute the total mass difference G, then redistribute the mass difference of liquid phase G_1 uniformly to the interfacial transition layer that belongs to this phase and redistribute the counterpart

Algorithm 1 The mass compensation algorithm.

1. Set initial values ϕ_h^0, $\mathbf{u}_h^0$, p_h^0, p_h^{-1}, ρ_h^0, η_h^0, $l_{s_h}^0$, and $t = 0$.
2. Compute the initial total mass: $M^0 = \int_{\Omega_h} \phi_h^0 \mathrm{d}\Omega$, and the initial mass for phase 1: $M_1^0 = \int_{\phi_h^0 \geq 0} \phi_h^0 \mathrm{d}\Omega$.
3. Loop in time for $n = 0, \cdots$
   (a) Solve the Cahn–Hilliard equation according to (21)–(22).
   (b) Set initial values $\hat{\phi}_h^0 = \phi_h^{n+1}$.
   (c) For $k = 1, \cdots$ do:
      (i) Truncate the undershoot/overshoot values:

$$\hat{\phi}_h^k = \begin{cases} 1, & \hat{\phi}_h^{k-1} > 1, \\ -1, & \hat{\phi}_h^{k-1} < -1, \\ \hat{\phi}_h^{k-1}, & \text{else.} \end{cases}$$

      (ii) Compute the total mass: $M = \int_{\Omega_h} \hat{\phi}_h^k \mathrm{d}\Omega$ and the mass for phase 1: $M_1 = \int_{\hat{\phi}_h^k \geq 0} \hat{\phi}_h^k \mathrm{d}\Omega$.
      (iii) Compute the mass difference of phase 1: $G_1 = M_1^0 - M_1$ and the total mass difference $G = M^0 - M$.
      (iv) Compute the volume of the interfacial transition layer that belongs to phase 1: $V_1 = \int_{\Omega_h^1} \mathrm{d}\Omega$ and phase 2: $V_2 = \int_{\Omega_h^2} \mathrm{d}\Omega$, where $\Omega_h^1 := \{(x, y, z) \in \Omega_h : 0 \leq \hat{\phi}_h^k(x, y, z) < 1\}$ and $\Omega_h^2 := \{(x, y, z) \in \Omega_h : -1 < \hat{\phi}_h^k(x, y, z) < 0\}$.
      (v) Uniformly distribute G_1 over Ω_h^1 and $G - G_1$ over Ω_h^2:

$$\hat{\phi}_h^k = \begin{cases} \hat{\phi}_h^k + G_1/V_1, & (x, y, z) \in \Omega_h^1, \\ \hat{\phi}_h^k + (G - G_1)/V_2, & (x, y, z) \in \Omega_h^2, \\ \hat{\phi}_h^k, & \text{else.} \end{cases}$$

      (vi) If $\|\hat{\phi}_h^k - \hat{\phi}_h^{k-1}\|_\infty < 10^{-8}$, break.
   end do
   (d) Reset $\phi_h^{n+1} = \hat{\phi}_h^k$.
   (e) Update ρ_h^{n+1}, η_h^{n+1}, and $l_{s_h}^{n+1}$ according to (23).
   (f) Solve the velocity system of Navier–Stokes equations according to (24).
   (g) Solve the pressure system of Navier–Stokes equations according to (25).
   end time loop

$G - G_1$ uniformly to that belongs to the other phase. An iterative process is applied in order to avoid reproducing new undershoot/overshoot such that the converged solution is guaranteed to be within $[-1, 1]$. The iteration continues until the phase variable stops changing within the given tolerance (i.e., 10^{-8} for our applications). Our numerical results show that this algorithm can preserve the mass of the droplet even in the case of small volume ($1\% \sim 6\%$ of the domain), large density ratio, and large viscosity ratio.

3.4. Scalable solution algorithm

Preconditioned Krylov subspace solvers are used to obtain the solutions of different systems in each time step. Specifically, systems arising from implicit discretization of the Cahn–Hilliard equation (Step 1) and the velocity equation (Step 3) are solved by a restricted additive Schwarz (RAS [3]) preconditioned GMRES method, and the pressure Poisson system (Step 4) is solved by an algebraic multigrid (AMG) preconditioned CG method. The overall algorithm is implemented on a parallel computer with distributed memory. Let np be the number of processors, we partition the finite element mesh into np subdomains using a graph-based partitioning approach (MeTis [16]) and each vertex of the graph represents an element of the mesh: $\Omega_h = \Omega_{h,1} \cup \cdots \cup \Omega_{h,np}$ where $\Omega_{h,i} \cap \Omega_{h,j} = \emptyset$ for all $i \neq j$. A computational domain with a rough surface and sample partition into 24 subdomains are shown in Fig. 3. The algorithms are implemented using libMesh [17] for generating the stiffness matrices, and PETSc [1] for the preconditioned Krylov subspace solvers. Unstructured meshes are generated using Gmsh [11] for all cases such that near the bottom boundary and the initial position of the droplet the mesh size is finer. In general, the mesh size is $4 \sim 6$ times finer than the size of the micrometric roughness.

4. Results and discussion

4.1. Coalescence of two droplets on a flat hydrophilic surface

For the first case, to verify the effectiveness of the proposed finite element scheme as well as the mass compensation algorithm, we simulate the dynamics of two interacting droplets on a flat hydrophilic surface. Due to the effect of surface tension, the two droplets coalesce into one with the shape evolves to be a spherical cap. The computational domain is $[-0.25, 0.25] \times [-0.4, 0.4] \times [-0.4, 0.4]$ and a structured mesh with $50 \times 80 \times 80$ elements is used. Two half-sphere droplets

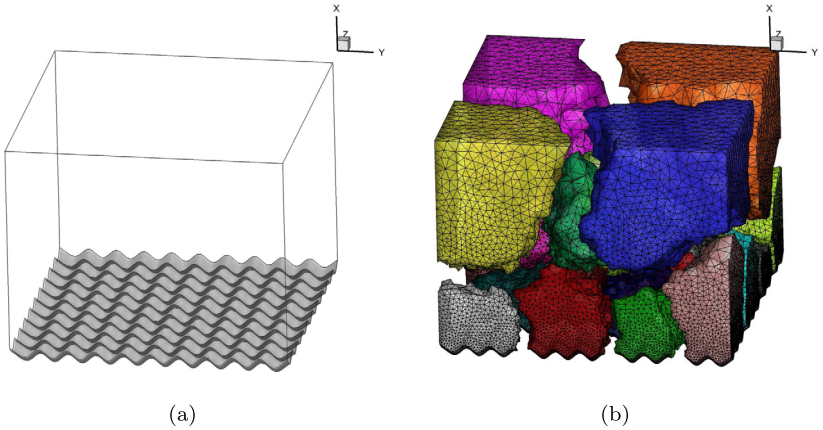

Fig. 3. (a) A computational domain with a rough surface. (b) A sample partition into 24 subdomains.

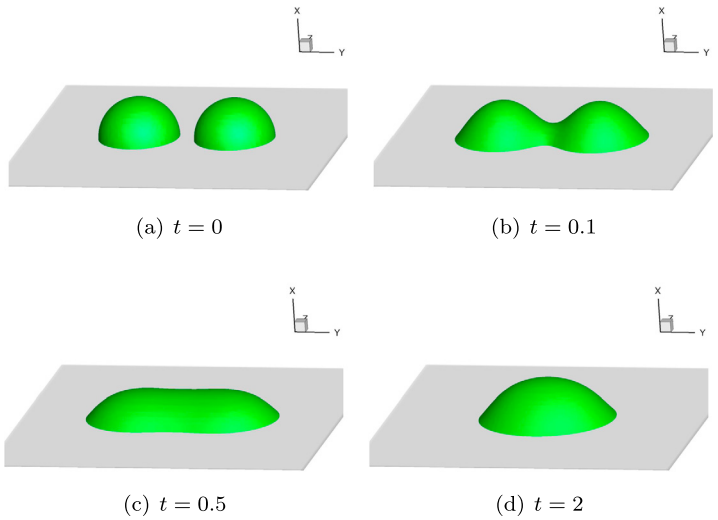

Fig. 4. Coalescence of two droplets on a flat hydrophilic surface. The static contact angle is $\theta_s^{surf} = 50°$.

with initial radius $r_0 = 0.1$ are initially located on the solid surface. The distance between the two centers is 0.24. We assume that the size of the droplet is small so that the gravity is negligible [6]. The static contact angle is $\theta_s^{surf} = 50°$ and the time step size is $\delta t = 0.1h = 0.001$. Other parameters used are as follows:

$$\lambda_\rho = 0.001, \quad \lambda_\eta = 0.01, \quad \lambda_{l_s} = 1, \quad Re = 3000, \quad \mathcal{L}_d = 5.0 \times 10^{-4},$$
$$\mathcal{B} = 40, \quad \mathcal{V}_s = 500, \quad \mathcal{L}_s = 0.038, \quad s = 1.5, \quad \tilde{\alpha} = 0.374, \quad \epsilon = 0.01.$$

In general, these parameters should be chosen depending on the particular simulation cases. In this paper, $\mathcal{L}_d$, $\mathcal{V}_s$, $\mathcal{L}_s$, s, and $\tilde{\alpha}$ are chosen the same as in Gao and Wang [10], where the same model was used to simulate droplet spreading on a flat patterned surface. We reuse these parameters later to study droplet spreading on rough surfaces.

Fig. 4 shows the snapshots of the merging process at different times. To check the convergence of the method, we study the impact of time step length and mesh size on the droplet shape. Results are shown in Fig. 5. It is clear that the results converge with the time reduction and mesh refinement. In Fig. 6, results obtained using the mass compensation algorithm are compared to those obtained using the treatment introduced by Chiu and Lin [5]. In this experiment, the droplets occupy only 1.309% of the total volume of the computational domain and the initial radius is smaller than the critical radius $r_c = 0.1397$. We define the relative difference of the total mass of ϕ as

$$D_{total} = \left| \frac{\int_\Omega \phi_h^0 \mathrm{d}\Omega - \int_\Omega \phi_h^n \mathrm{d}\Omega}{\int_\Omega \phi_h^0 \mathrm{d}\Omega} \right|,$$

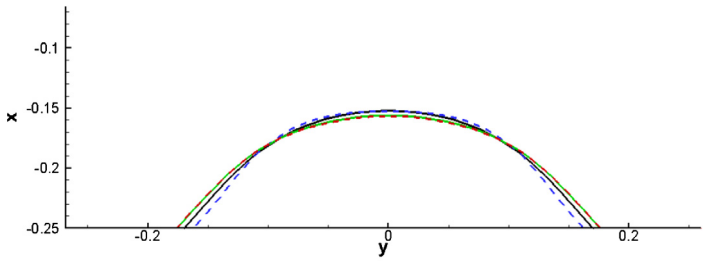

(a) Comparison of different time step length. Blue dashed: $\delta t = 0.002$, black solid: $\delta t = 0.001$, green solid: $\delta t = 0.0005$, red dashed: $\delta t = 0.00025$. A structured mesh with $50 \times 80 \times 80$ elements is used.

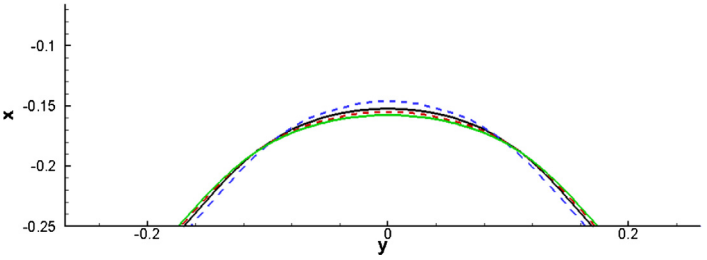

(b) Comparison of different meshes. Blue dashed: $40 \times 60 \times 60$ elements, black solid: $50 \times 80 \times 80$ elements, red dashed: $60 \times 100 \times 100$ elements, green solid: $70 \times 120 \times 120$ elements. $\delta t = 0.001$.

Fig. 5. Impact of time step length and mesh size on the droplet shape at $t = 2$. The zero contour of ϕ is shown at slice $z = 0$. (For interpretation of the references to color in this figure legend, the reader is referred to the web version of this article.)

Table 1
Computational domain and mesh information of Case i–iii.

Case	Specification of posts	Elements	Nodes
i	$l = 0.2$, $w = 0.1$, $d = 0.04$	4,045,224	727,950
ii	$l = 0.1$, $w = 0.1$, $d = 0.04$	3,577,224	635,398
iii	$l = 0.2$, $w = 0.16$, $d = 0.04$	3,905,112	684,203

and the relative difference of the mass of ϕ belongs to the droplet as

$$D_{droplet} = \left| \frac{\int_{\phi_h^0 \geq 0} \phi_h^0 \mathrm{d}\Omega - \int_{\phi_h^n \geq 0} \phi_h^n \mathrm{d}\Omega}{\int_{\phi_h^0 \geq 0} \phi_h^0 \mathrm{d}\Omega} \right|,$$

Fig. 7 shows the comparison of D_{total} and $D_{droplet}$ with respect to time. It is shown that with Chiu and Lin's treatment, although the total mass is conserved, the droplet shrinks spontaneously and eventually disappears. On the contrary, the proposed algorithm is capable to preserve both the total mass and the mass of the droplet.

4.2. A substrate with circular posts

In this case we study the dynamics of a droplet when it falls on a solid substrate that textured with circular posts. Each post is a pillar with length l and spacing w (see Fig. 8). The diameter of each pillar d is fixed to 0.04. The computational domain is $[-l, 1.2] \times [0, 0.5\pi] \times [0, 0.5\pi]$. Table 1-i shows the mesh information. In the middle of the domain, a spherical droplet with radius 0.3 falls freely from a height 0.35 (from the center of the droplet to the top of posts):

$$\phi|_{t=0} = -\tanh\left(\frac{\sqrt{(x-0.35)^2 + (y-0.25\pi)^2 + (z-0.25\pi)^2} - 0.3}{\sqrt{2}\epsilon} \right),$$

where $\epsilon = 0.02$. The initial speed of the droplet is $(-1, 0, 0)$. The gravity is neglected in this subsection. The static contact angle is taken as $\theta_s^{surf} = 130^\circ$ that represents the hydrophobic property of the posts. The Reynolds number is $Re = 300$ and the time step size is $\delta t = 0.0008$. All the other parameters are taken as in Section 4.1.

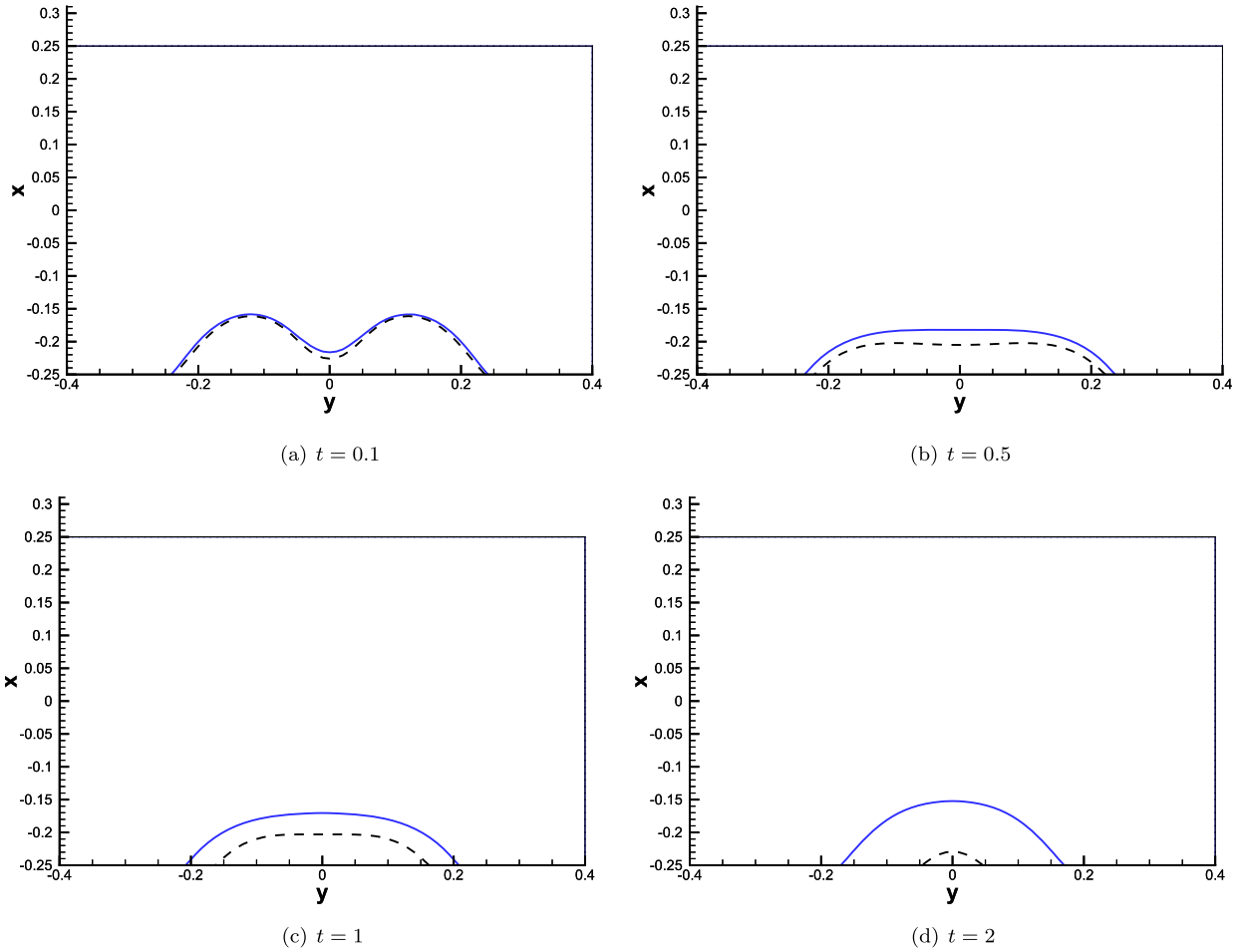

(a) $t = 0.1$ (b) $t = 0.5$

(c) $t = 1$ (d) $t = 2$

Fig. 6. Comparison of results at slice $z = 0$ obtained by using the new mass compensation method and Chiu and Lin's treatment [5]. The static contact angle is $\theta_s^{surf} = 50°$. Blue solid: using the new mass compensation method; black dashed: using Chiu and Lin's treatment.

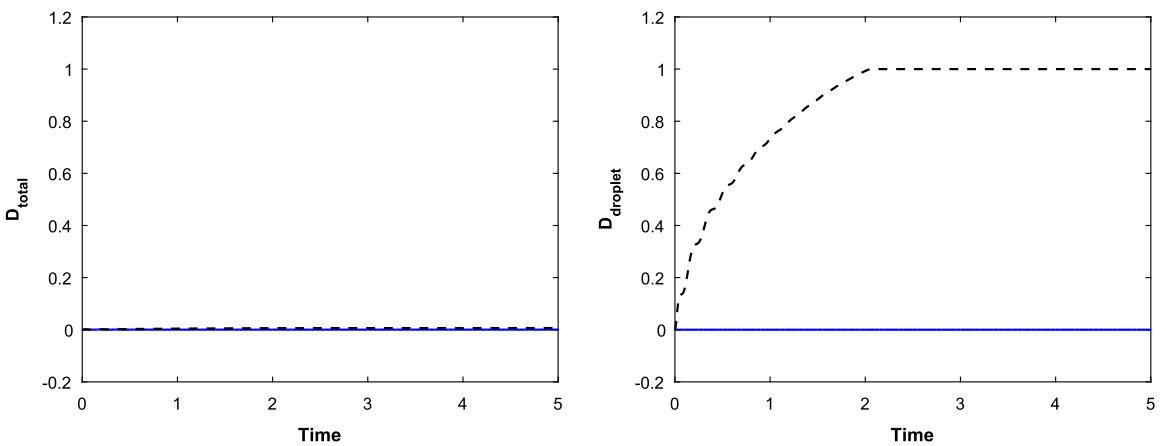

(a) D_{total} (b) $D_{droplet}$

Fig. 7. (a) The relative difference of the total mass of ϕ (D_{total}), and (b) the relative difference of the mass of ϕ belongs to the droplet ($D_{droplet}$). Blue solid: using the mass compensation method; black dashed: using Chiu and Lin's treatment.

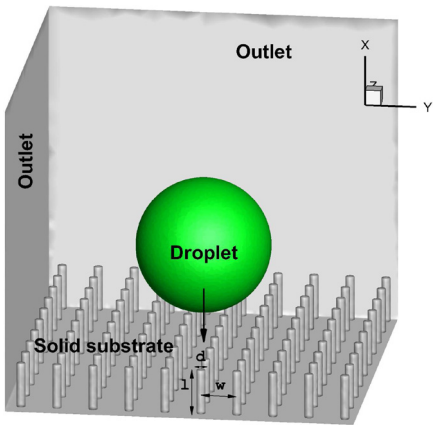

Fig. 8. The domain where a droplet falls on a substrate with hydrophobic posts. Each post is a circular pillar with length l and spacing w. The diameter of each pillar d is fixed to 0.04.

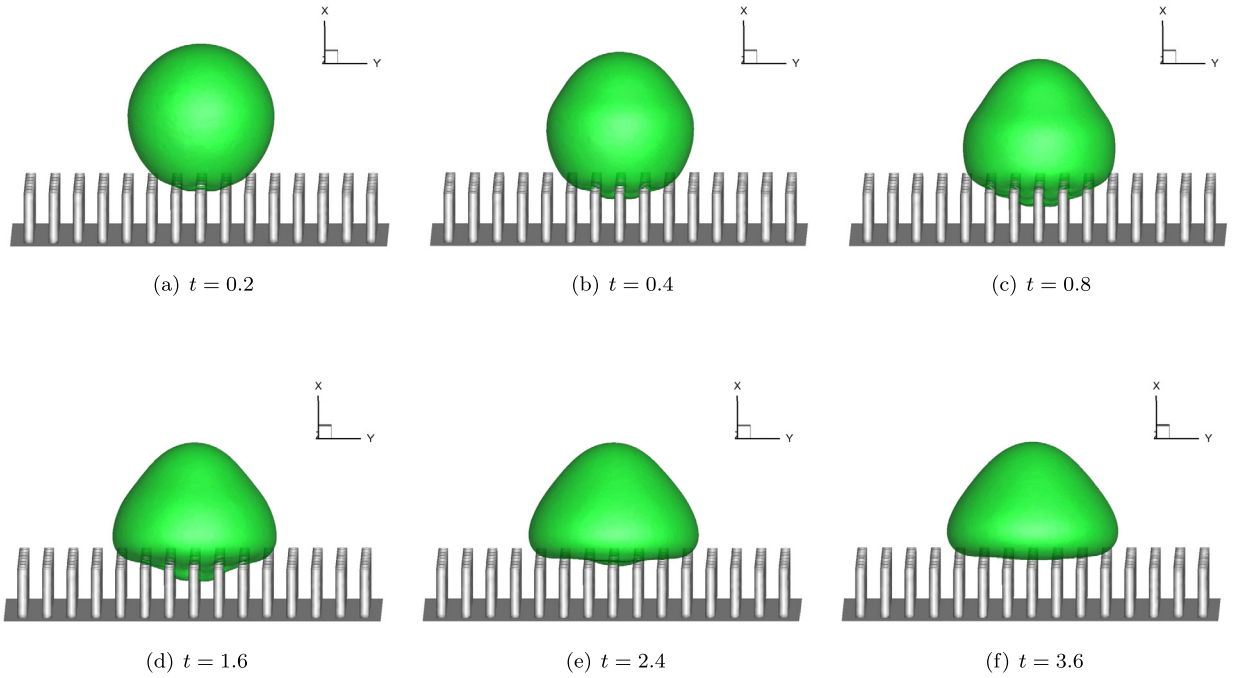

(a) $t = 0.2$ (b) $t = 0.4$ (c) $t = 0.8$

(d) $t = 1.6$ (e) $t = 2.4$ (f) $t = 3.6$

Fig. 9. Dynamics of a droplet falling on a solid surface textured with circular posts: (Case i) $l = 0.2$, $w = 0.1$ and $d = 0.04$. The static contact angle is $\theta_s^{surf} = 130°$.

The phenomenon of superhydrophobicity can be observed for certain height and spacing of the posts, for instant, Case i: $l = 0.2$ and $w = 0.1$. Fig. 9 shows several snapshots of the droplet at different time $t = 0.2, 0.4, 0.8, 1.6, 2.4$, and 3.6. With downward momentum, the droplet no longer keeps the shape of a sphere and spreads laterally when it touches the top of the posts. The microstructures on the solid surface can entrap air pockets, resulting in a composite surface that exhibits superhydrophobic properties. The dynamics of the droplet can be classified into two stages: (a) the infiltrating stage and (b) the recoiling stage, as shown in the slice view at $z = 0$ in Fig. 10. During the infiltrating stage, the droplet wets the top of central post and propagates into the grooves, forming a liquid infiltration. This stage continues till the downward momentum is completely dissipated. Afterward the infiltration starts to recoil because of the surface tension, slowly dewetting the posts. The droplet has a much larger apparent contact angle compared to that on a smooth surface, which is known as the Cassie state.

It is well known that varying the size and spacing of the posts can considerably affect the dynamics of the droplet and may lead to a Wenzel state. We consider two variations of the posts: a shorter length in Case ii: $l = 0.1$, $w = 0.1$; and a larger spacing in Case iii: $l = 0.2$, $w = 0.16$ (see Table 1-ii,iii). For comparison, snapshots of the droplet for these two cases during the same time period are shown in Fig. 11 and Fig. 12. It is found that if the posts are shorter, the droplet

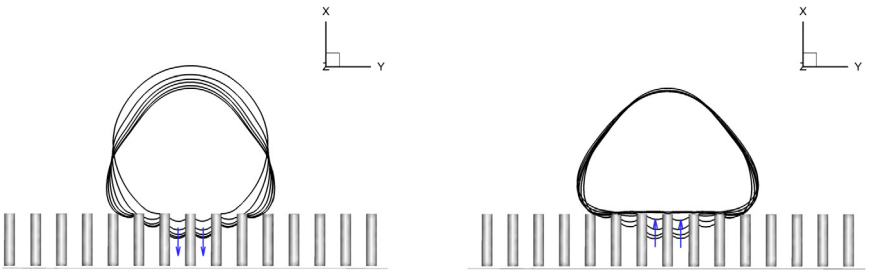

(a) The infiltrating stage (b) The recoiling stage

Fig. 10. Slice view at $z = 0$ for dynamics of a droplet falling on a solid surface textured with circular posts: (Case i) $l = 0.2$, $w = 0.1$ and $d = 0.04$. The static contact angle is $\theta_s^{surf} = 130°$. (a) The infiltrating stage, (b) the recoiling stage.

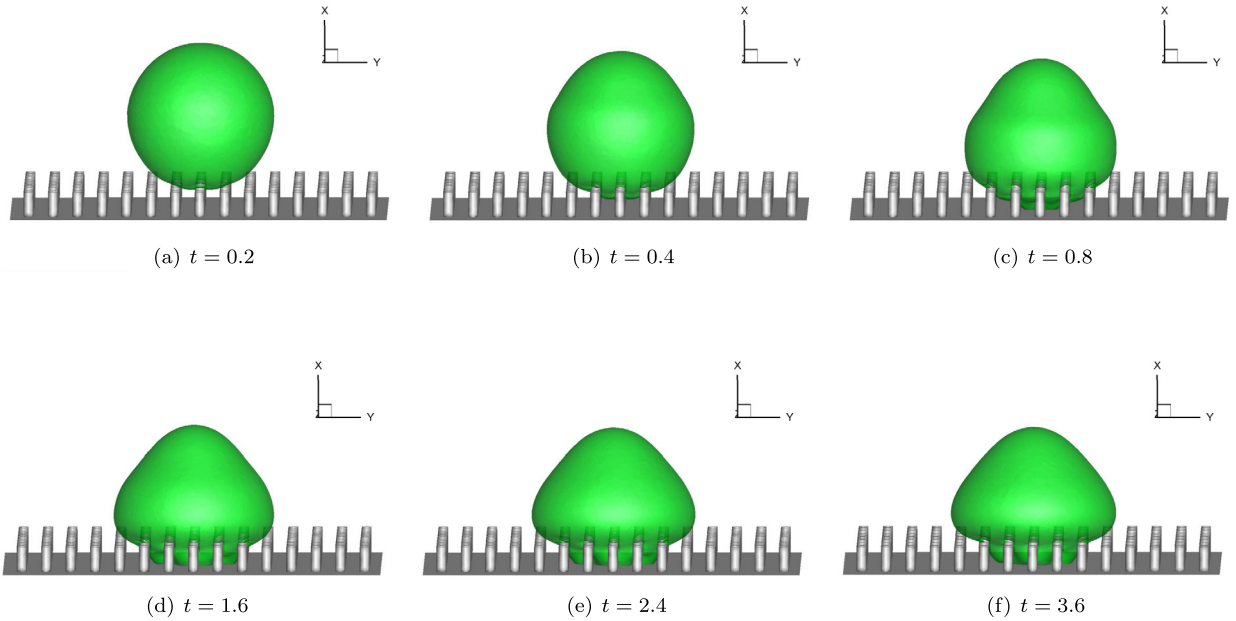

(a) $t = 0.2$ (b) $t = 0.4$ (c) $t = 0.8$

(d) $t = 1.6$ (e) $t = 2.4$ (f) $t = 3.6$

Fig. 11. Dynamics of a droplet falling on a solid surface textured with circular posts: (Case ii) $l = 0.1$, $w = 0.1$, and $d = 0.04$. The static contact angle is $\theta_s^{surf} = 130°$.

Table 2
Computational domain and mesh information of Case 1 and Case 2.

Case	$b(y, z)$	Parameters	Elements	Nodes
1	$0.025\sin(40y)$	$y \in [0, 0.5\pi]$	3,160,792	554,093
2	$0.025\cos(40y)\cos(40z)$	$y, z \in [0, 0.5\pi]$	3,289,936	576,663

will touch the bottom surface, resulting in a Wenzel state. On the other hand, when the spacing between posts is larger, partial infiltration of liquid can propagate deeply into the grooves and wet the bottom surface, leading to a Cassie–Wenzel transition.

4.3. Surfaces textured with parallel strips and periodic waves

We next study the contact line motion of a droplet spreading over various rough surfaces. The CAH proves to be an important quantity that determines the motion and properties of the surfaces. To understand how the roughness affects the CAH and the contact line motion is of critical importance in surface engineering. We focus on dynamical hysteresis in 3D, particularly those not captured by 2D static models. Two types of surfaces are considered including parallel strips (Case 1) and periodic waves (Case 2). The computational domain is $[b(y, z), 1.2] \times [0, 0.5\pi] \times [0, 0.5\pi]$, where the bottom topology $b(y, z)$ and the mesh information are listed in Table 2. The static contact angle for these two cases is $\theta_s^{surf} = 50°$ that represents the hydrophilic property of the surfaces. All the other parameters are taken as in Section 4.1. The initial configuration for these two cases is the same as in Section 4.2. The gravity is also neglected in this subsection.

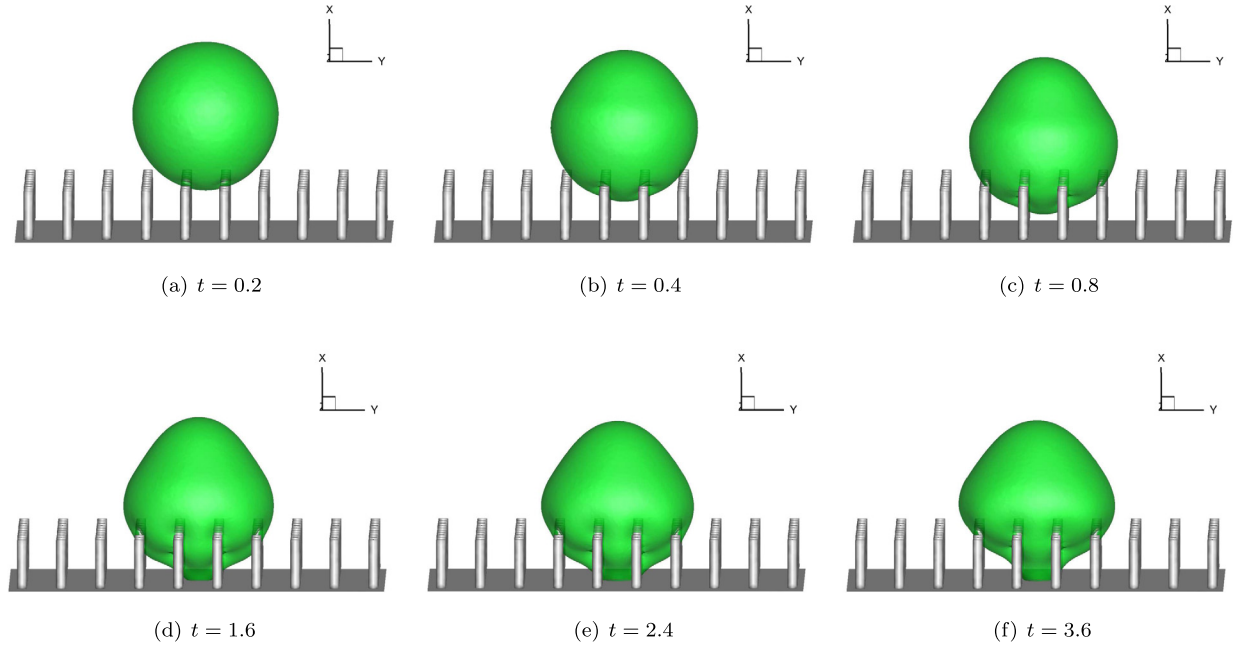

Fig. 12. Dynamics of a droplet falling on a solid surface textured with circular posts: (Case iii) $l = 0.2$, $w = 0.16$, and $d = 0.04$. The static contact angle is $\theta_s^{surf} = 130°$.

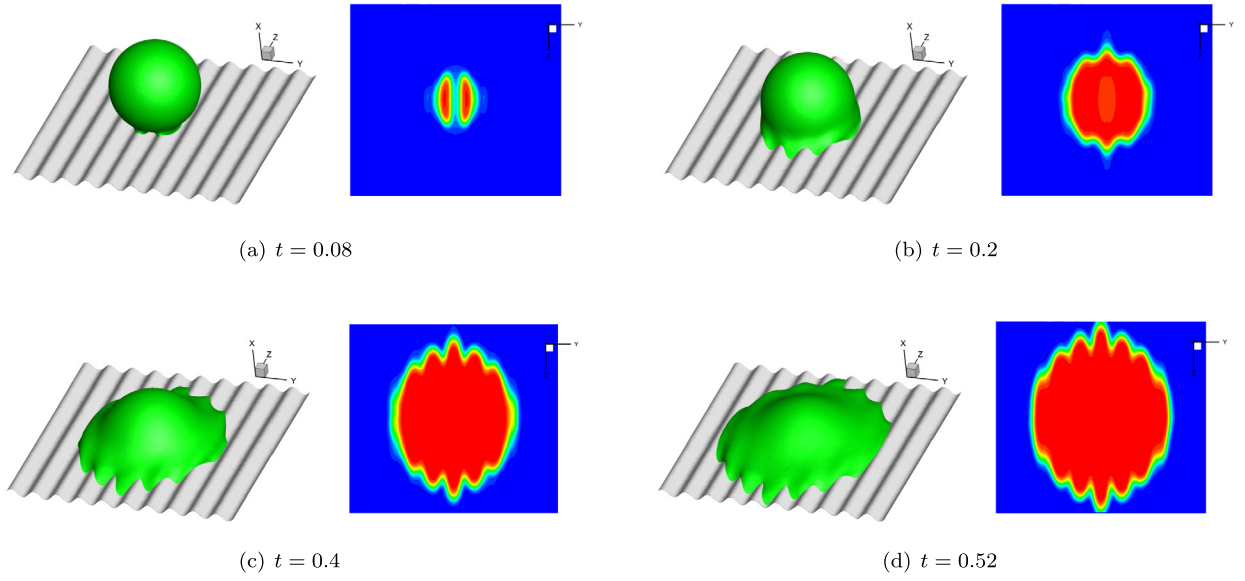

Fig. 13. Dynamics of a droplet spreading on a solid surface textured with parallel strips (Case 1: $b(y, z) = 0.025\sin(40y)$, $y \in [0, 0.5\pi]$). The corresponding bottom projection view for the contour of ϕ are also listed on the right.

Dynamics of the droplet at different time for Case 1 are shown in Fig. 13. The corresponding bottom projection views for the contour of ϕ are also listed on the right. The interface shows strong deformation as the front of the surface passes though the wavy strips along the y-axis. The spreading diameter of droplet along this direction is smaller than along the z-axis. The wavy patten along the z-axis explicitly reflects the geometry of the surface. Such an anisotropic behavior can only be observed in a complete 3D simulation. The contact line motion is shown in Fig. 15 (a).

In Case 2, the solid surface is parametrized by a periodic sinusoidal function. Different from Case 1, the droplet will experience wavy texture along all directions thus its spreading may assume a variety of shapes. Dynamics of the droplet and the bottom projection views are shown in Fig. 14. It is shown that the contact lines on the "uphill" regions are concave while those on the "downhill" regions are convex. CAH can be easily found from the top view of contact lines in Fig. 15 (b).

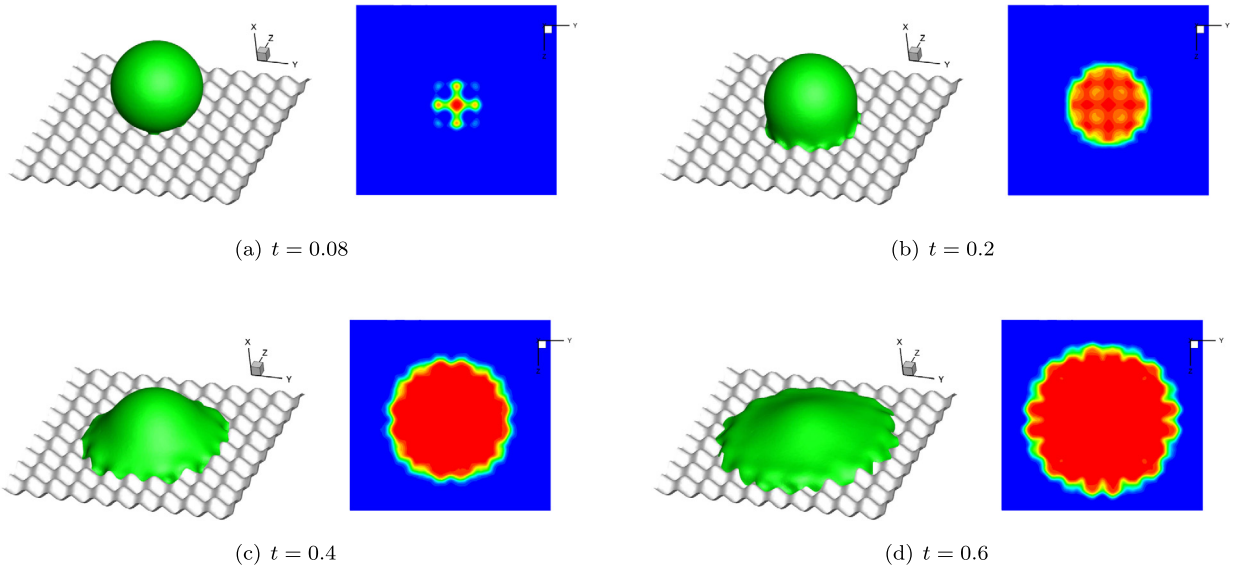

(a) $t = 0.08$ (b) $t = 0.2$

(c) $t = 0.4$ (d) $t = 0.6$

Fig. 14. Dynamics of a droplet spreading on a solid surface textured with periodic waves (Case 2: $b(y, z) = 0.025\cos(40y)\cos(40z)$, $y, z \in [0, 0.5\pi]$). The corresponding bottom projection view for the contour of ϕ are also listed on the right.

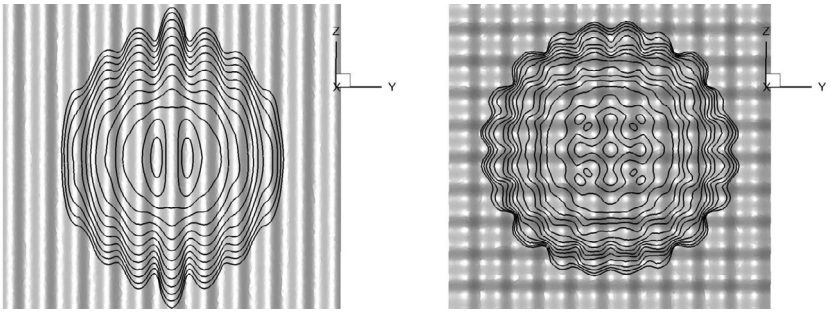

(a) Case 1 (b) Case 2

Fig. 15. Top views of contact line motion for a droplet spreading on a solid surface textured with parallel strips or periodic waves.

When moving along one particular direction, the front of the interface exhibits both of the concave and convex shapes alternatively, depending on the region it achieves.

4.4. An inclined surface with a large variation of wavy shape

In this numerical experiment we consider the dynamics of a droplet moving on an inclined surface with a large variation of wavy shape, as shown in Fig. 16. The computational domain is $[\cos(20y)\cos(20z), 8] \times [0, 5\pi] \times [0, 5\pi]$ with $y, z \in [0, 5\pi]$ and the unit is 1 mm. The inclination is encoded via a rotation of the domain with angle 60°. The mesh has 3,660,320 elements and 648,023 nodes. A spherical droplet with diameter 4 mm falls freely with downward speed 0.5 m/s. The initial center of the droplet is (4.5 mm, 2.5π mm, 2.5π mm). The densities for the liquid and air are 0.998×10^3 kg/m^3 and 1.205 kg/m^3, the viscosities for the liquid and air are 1.002×10^{-3} Pa·s and 1.511×10^{-5} Pa·s. The interfacial tension is $\gamma = 0.075$ N/m. For this case we take the gravity $g = 9.81$ m/s^2 into account. By taking the characteristic length as 10 mm and the characteristic velocity as 0.5 m/s, we obtain the following dimensionless numbers: $\lambda_\rho = 1.207 \times 10^{-3}$, $\lambda_\eta = 1.508 \times 10^{-2}$, $Re = 4980.04$, $\mathcal{B} = 158.781$, and the Froude number $Fr = 1.596$. We consider both the hydrophilic and hydrophobic properties by setting the static contact angle as 30° and 150°. Other parameters are taken as follows:

$$\mathcal{L}_s = 0.038, \quad \lambda_{l_s} = 1, \quad \mathcal{L}_d = 5.0 \times 10^{-4}, \quad \mathcal{V}_s = 500,$$
$$\epsilon = 0.02, \quad s = 1.5, \quad \tilde{\alpha} = 0.374, \quad \delta t = 0.002.$$

The initial conditions for ϕ is

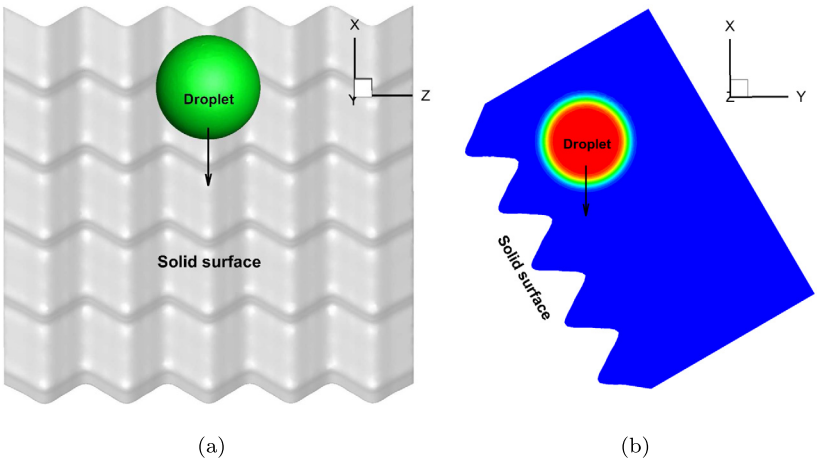

Fig. 16. (a) The domain where a droplet moves on an inclined surface with a large variation of wavy shape: $b(y,z)=\cos(20y)\cos(20z)$, $y,z\in[0,0.5\pi]$ and the unit is 1 mm. The inclination angle is 60°. (b) A slice view of $z=0$ for the contour plot of ϕ.

$$\phi|_{t=0}=-\tanh\left(\frac{\sqrt{(x-0.45)^2+(y-0.25\pi)^2+(z-0.25\pi)^2}-0.2}{\sqrt{2}\epsilon}\right),$$

and the initial speed of the droplet is $(-1,0,0)$.

The geometry of the surface consists of isolated peaks and crossing channels, and the magnitude of which is large enough to topologically change the global shape of the droplet. The dynamics for the hydrophilic case at different time are shown in Fig. 17. The slice views at $z=0$ are also listed on the right. With downward momentum and the gravitational force, the liquid flows downward along the middle channel and fills each valley of it. When the front of the interface reaches the gap between two peaks, the liquid propagates through the gap and wets the horizontal valleys on both sides, due to the attractive effect of the hydrophilic surface. The dynamics for the hydrophobic case together with the slice views at $z=0$ are shown in Fig. 18. In contrast to the hydrophilic case, the liquid does not adhere to the surface but moves down along the middle channel with small pockets of air entrapped beneath it. The hydrophobic property of the surface provides a mechanism to prohibit the droplet wetting the neighbor valleys. These results show that the droplet motion depends on the composition of the surface geometry and the material characteristic.

4.5. Spreading process of an impacting droplet on a microstructured surface

In this numerical experiment, we study a typical case in Sivakumar et al. [26] with specific surface texture and flow condition. The computational domain is $[-0.3,6]\times[0,15]\times[0,15]$ and the unit is 1 mm. The mesh has 2,660,368 elements and 497,771 nodes. The bottom surface is textured with circular posts with height 0.3 mm, diameter 0.3 mm, and spacing 0.6 mm. A spherical droplet with diameter 3 mm falls freely with downward speed 1.9626 m/s. The initial center of the droplet is (1.56 mm, 7.5 mm, 7.5 mm). The densities for the liquid and air are 1000 kg/m^3 and 1 kg/m^3, the viscosities for the liquid and air are 10^{-3} Pa·s and 10^{-5} Pa·s. The interfacial tension is $\gamma=0.073$ N/m. The gravity $g=9.8$ m/s^2 is taken into account. By taking the characteristic length as 3 mm and the characteristic velocity as 1.9626 m/s, we obtain the following dimensionless numbers: $\lambda_\rho=10^{-3}$, $\lambda_\eta=10^{-2}$, $Re=5887.8$, $\mathcal{B}=39.45$, and the Froude number $Fr=11.45$. These values correspond to $We=158.3$ and $Oh=0.00214$ in cases shown by Fig. 5 and Fig. 15(b) of Sivakumar et al. [26]. The static contact angle is taken as 150°. Other parameters are taken as follows:

$$\mathcal{L}_s=0.038,\quad \lambda_{l_s}=1,\quad \mathcal{L}_d=5.0\times10^{-5},\quad \mathcal{V}_s=500,$$
$$\epsilon=0.05,\quad s=1.5,\quad \tilde{\alpha}=0.374,\quad \delta t=0.0005.$$

The initial conditions for ϕ is

$$\phi|_{t=0}=-\tanh\left(\frac{\sqrt{(x-0.52)^2+(y-2.5)^2+(z-2.5)^2}-0.5}{\sqrt{2}\epsilon}\right),$$

and the initial speed of the droplet is $(-1,0,0)$.

Fig. 19 shows the time-lapsed image sequence for the impact of the droplet on the microstructured substrate. An overall agreement is achieved between the numerical and experimental results. It is observed from Fig. 20 that the liquid volume spreading inside the grooves does not fill the grooves entirely but flows like thin liquid jets. As indicated by Sivakumar et al. [26], the texture geometry influences the spreading process and develops spreading patterns, which are dramatically different from those observed on a smooth surface.

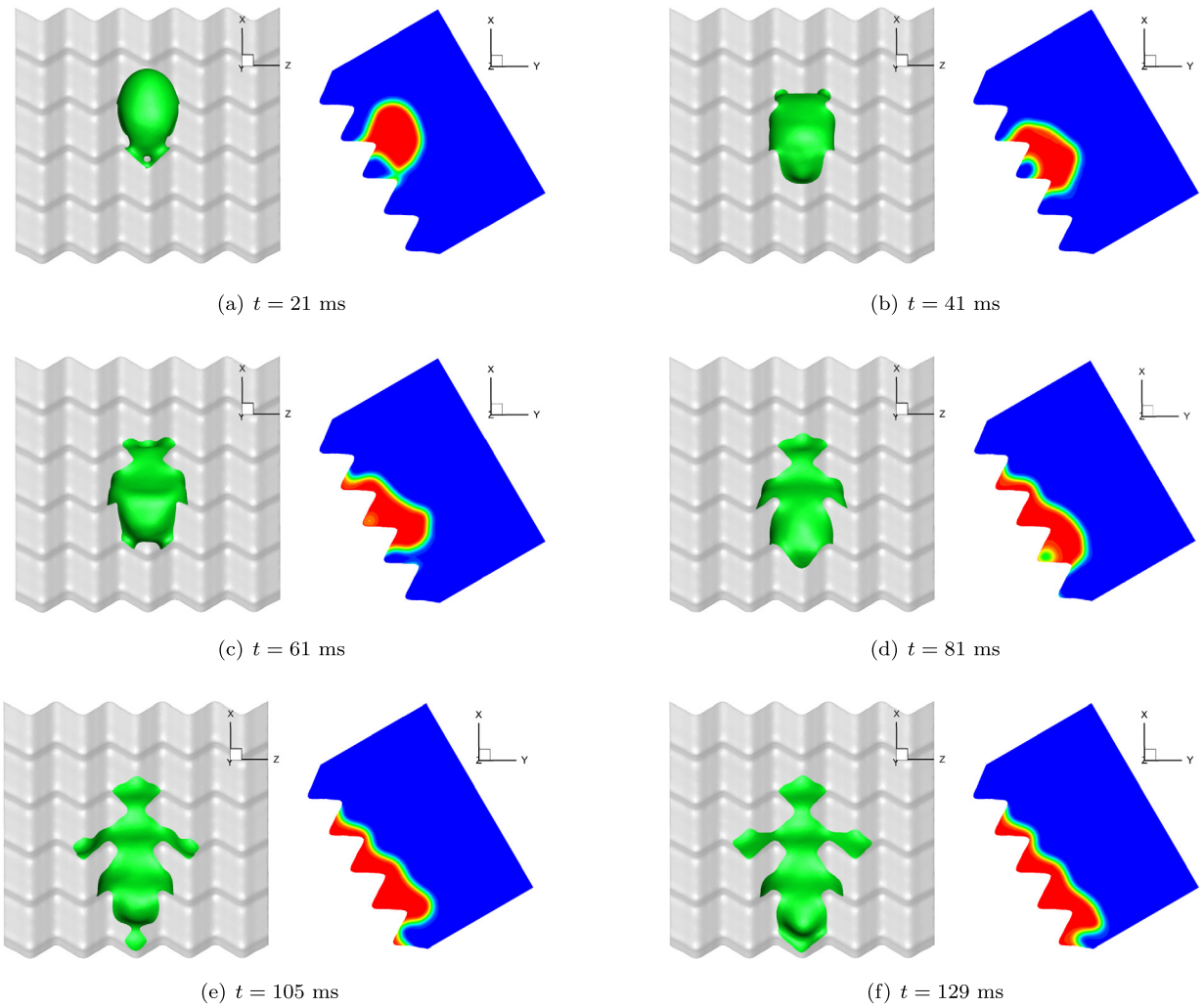

(a) $t = 21$ ms (b) $t = 41$ ms

(c) $t = 61$ ms (d) $t = 81$ ms

(e) $t = 105$ ms (f) $t = 129$ ms

Fig. 17. Dynamics of a droplet moving on a hydrophilic inclined surface with a large variation of wavy shape: $b(y, z) = \cos(20y)\cos(20z)$, $y, z \in [0, 0.5\pi]$ and the unit is 1 mm. The corresponding slice views of $z = 0$ for the contour plot of ϕ are also listed on the right. The surface is tilted with 60° and the static contact angle is $\theta_s^{surf} = 30°$.

4.6. Parallel performance

In this section, we report the scalability and parallel speedup of the proposed solution algorithm for Case 2 in Section 4.3. The scalability tests are performed on the Tianhe 2 supercomputer. There are 24 processors and 64 GB memory on each node of Tianhe 2. We denote by "dof" the number of unknowns, "np" the number of processors, "GMRES" ("CG") the average number of GMRES (CG) iterations per time step, "sp." the speedup, and "Eff." the parallel efficiency. All timings are reported in seconds. The restart value of GMRES is fixed at 50. 10^{-8} is used as the relative stopping condition for linear solvers. The unstructured mesh has 212,434,560 elements and 31,711,677 vertices. For the additive Schwarz preconditioned GMRES solver, an incomplete LU (ILU) factorization with two and three fill-ins is used for the subdomain solver of the Cahn–Hilliard system and velocity system, respectively. For the AMG preconditioned CG solver of the pressure system, we use two sweeps of a Gauss–Seidel smoother. As shown in Table 3, the compute times reduce when the number of processors increases from 512 to 4,096, while the numbers of iterations do not change much, demonstrating good scalability and speedup for each system. Fig. 21 shows the total compute time, speedup, and parallel efficiency of the overall solution algorithm. The parallel efficiency is 78.5% when the number of processor cores is up to 4,096 which is reasonably good.

5. Conclusions

In this work we study the dynamics of a three-dimensional droplet spreading on topologically rough surfaces by numerical simulations. We adopt a phase-field model that consists of the coupled Cahn–Hilliard and Navier–Stokes equations with the generalized Navier boundary condition. A semi-implicit temporal scheme is introduced to fully decouple the phase func-

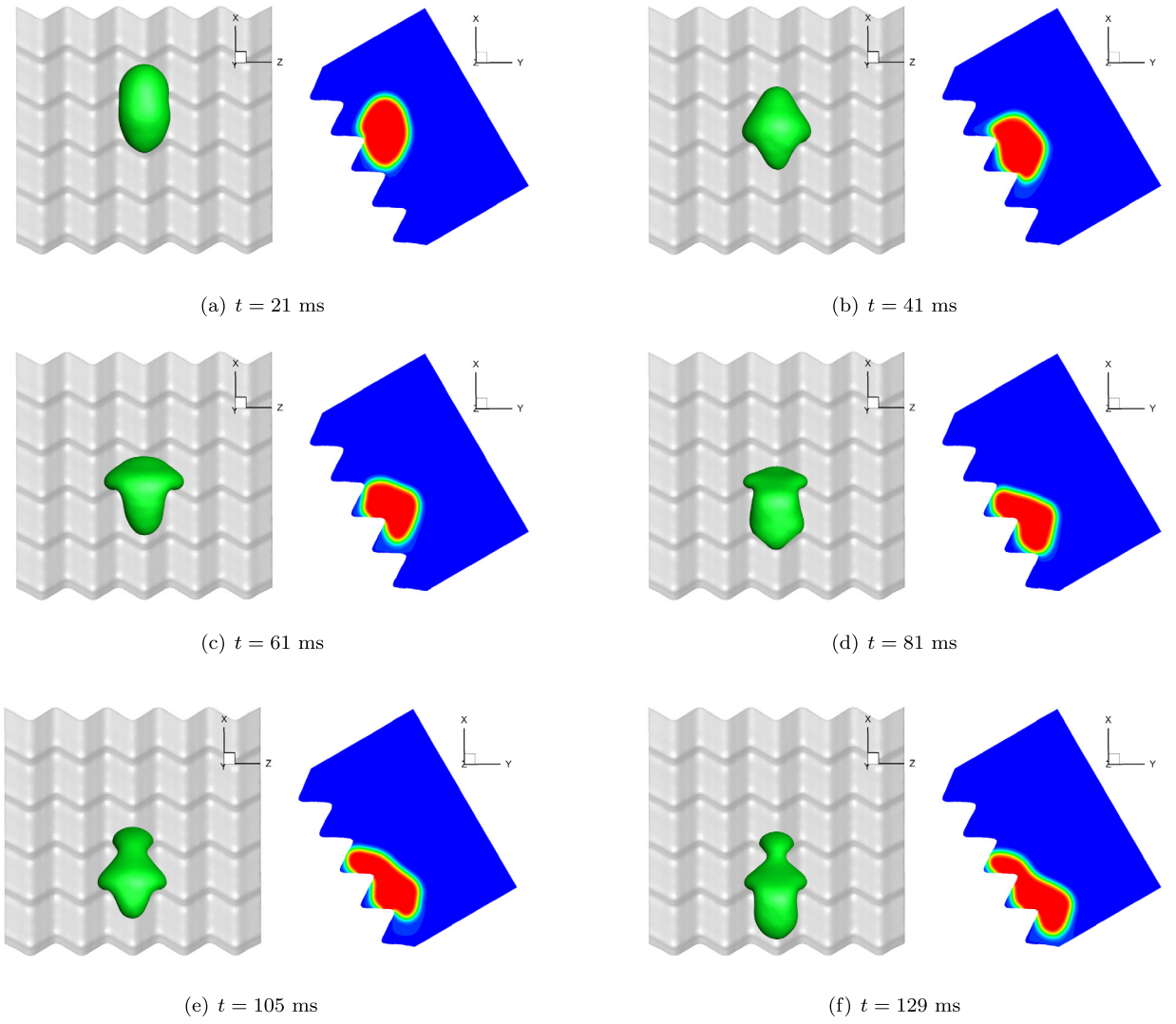

(a) $t = 21$ ms (b) $t = 41$ ms

(c) $t = 61$ ms (d) $t = 81$ ms

(e) $t = 105$ ms (f) $t = 129$ ms

Fig. 18. Dynamics of a droplet moving on a hydrophobic inclined surface with a large variation of wavy shape: $b(y, z) = \cos(20y)\cos(20z)$, $y, z \in [0, 0.5\pi]$ and the unit is 1 mm. The corresponding slice views of $z = 0$ for the contour plot of ϕ are also listed on the right. The surface is tilted with 60° and the static contact angle is $\theta_s^{surf} = 150°$.

Table 3
The scalability test for the proposed solution algorithm. The average number of GMRES (CG) iterations, compute time per time step, and speedup for solving the Cahn–Hilliard system, the velocity system, and the pressure system.

np	Cahn–Hilliard system dof = 63,423,354			velocity system dof = 95,135,031			pressure system dof = 31,711,677		
	GMRES	time(s)	sp.	GMRES	time(s)	sp.	CG	time(s)	sp.
512	8.1	12.68	1	9.3	23.27	1	30	11.88	1
1,024	7.4	6.48	1.96	9.8	11.88	1.96	30.4	6.46	1.84
2,048	8.4	3.45	3.68	9.6	6.65	3.50	32.3	3.56	3.34
4,096	8.3	1.87	6.78	10.1	3.71	6.27	31.1	2.0	5.94

tion, the velocity, and the pressure. An unstructured finite element discretization in space is employed to solve the problem with complex boundaries. In addition, a mass compensation algorithm is introduced to preserve the mass of the droplet. Numerical simulations are carried out to verify the effectiveness of our solver. Cassie and Wenzel states of the droplet can be observed on a solid substrate with posts. We also demonstrate CAH for a droplet spreading over various textures including parallel strips and periodic waves, as well as the wettability for a droplet flowing on an inclined surface with hydrophilic or hydrophobic property. Moreover, we study the spreading process of an impacting droplet on a microstructured surface.

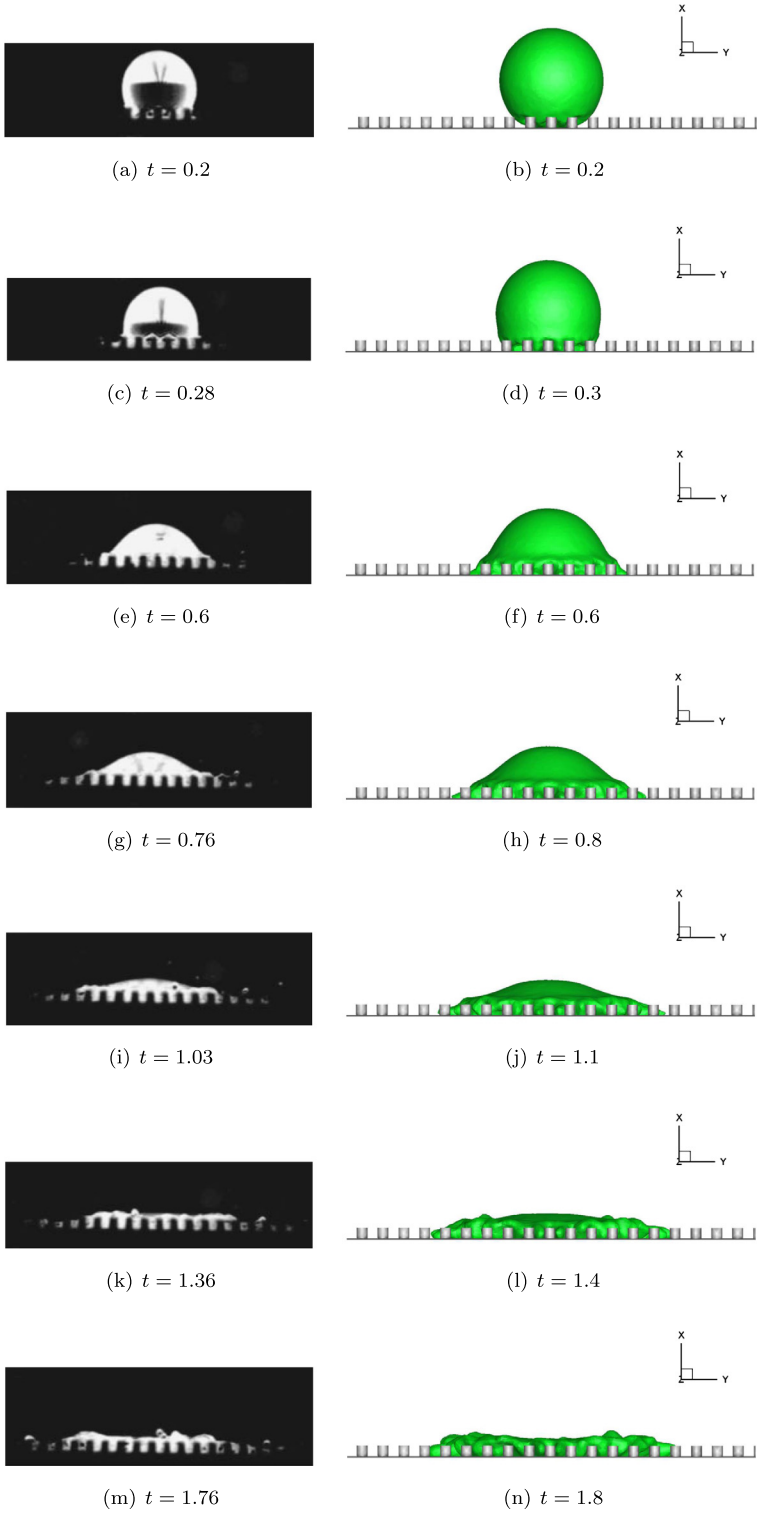

Fig. 19. Spreading of an impacting droplet on a microstructured surface with $l = 0.3$ mm, $d = 0.3$ mm, $w = 0.6$ mm, $Re = 5887.8$, $\mathcal{B} = 39.45$, $Fr = 11.45$. The left column is for the experimental results shown in Fig. 15(b) in Sivakumar et al. [26], the right column is for the numerical results.

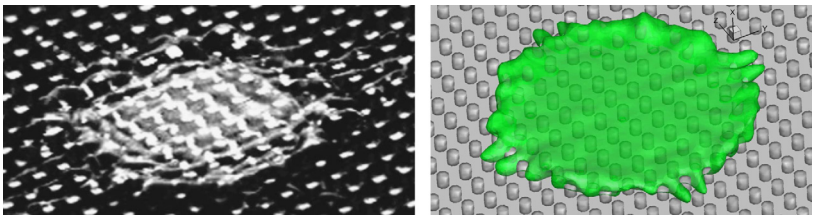

(a) Figure 5 in Sivakumar et al. [26], $t = 1.76$ (b) Numerical result at $t = 1.8$

Fig. 20. Comparison between the experimental and numerical results: jet spreading inside the grooves of the microstructured surface with $l = 0.3$ mm, $d = 0.3$ mm, $w = 0.6$ mm. $Re = 5887.8$, $\mathcal{B} = 39.45$, $Fr = 11.45$.

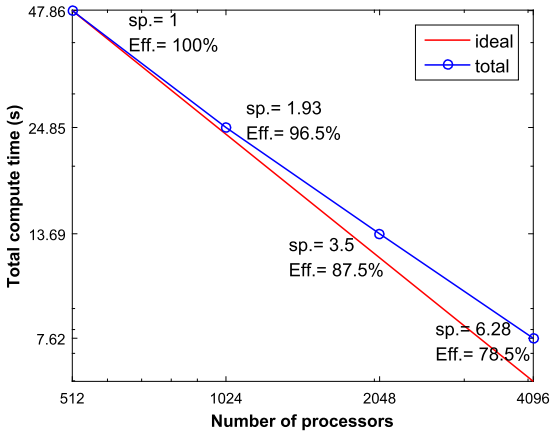

Fig. 21. Total compute time, speedup, and parallel efficiency for the overall solution algorithm.

A qualitative agreement is achieved between the numerical and experimental results. The results of parallel performance suggest that the solution algorithm scales well on supercomputer with a large number of processors.

References

[1] S. Balay, S. Abhyankar, M.F. Adams, J. Brown, P. Brune, K. Buschelman, V. Eijkhout, W.D. Gropp, D. Kaushik, M.G. Knepley, L.C. McInnes, K. Rupp, B.F. Smith, H. Zhang, PETSc Users Manual, http://www.mcs.anl.gov/petsc, Argonne National Laboratory, 2016.

[2] S. Brandon, N. Haimovich, E. Yeger, A. Marmur, Partial wetting of chemically patterned surfaces: the effect of drop size, J. Colloid Interface Sci. 263 (2003) 237–243.

[3] X.-C. Cai, M. Sarkis, A restricted additive Schwarz preconditioner for general sparse linear systems, SIAM J. Sci. Comput. 21 (1999) 792–797.

[4] X. Chen, X.-P. Wang, X. Xu, Effective contact angle for rough boundary, Physica D 242 (2013) 54–64.

[5] P.-H. Chiu, Y.-T. Lin, A conservative phase field method for solving incompressible two-phase flows, J. Comput. Phys. 230 (2011) 185–204.

[6] P.G. De Gennes, F. Brochard-Wyart, D. Quéré, A. Reisinger, B. Widom, Capillarity and Wetting Phenomena: Drops, Bubbles, Pearls, Waves, Springer, Berlin, 2004.

[7] V. Dussan, B. Elizabeth, S.H. Davis, On the motion of a fluid–fluid interface along a solid surface, J. Fluid Mech. 65 (1974) 71–95.

[8] C.W. Extrand, Model for contact angles and hysteresis on rough and ultraphobic surfaces, Langmuir 18 (2002) 7991–7999.

[9] D.J. Eyre, in: J.W. Bullard, et al. (Eds.), Computational and Mathematical Models of Microstructural Evolution, vol. 529, The Materials Research Society, 1998, pp. 39–46.

[10] M. Gao, X.-P. Wang, An efficient scheme for a phase field model for the moving contact line problem with variable density and viscosity, J. Comput. Phys. 272 (2014) 704–718.

[11] C. Geuzaine, J.-F. Remacle, Gmsh: a three-dimensional finite element mesh generator with built-in pre- and post-processing facilities, Int. J. Numer. Methods Eng. 79 (2009) 1309–1331.

[12] J.L. Guermond, A. Salgado, A splitting method for incompressible flows with variable density based on a pressure Poisson equation, J. Comput. Phys. 228 (2009) 2834–2846.

[13] B. He, N.A. Patankar, J. Lee, Multiple equilibrium droplet shapes and design criterion for rough hydrophobic surfaces, Langmuir 19 (2003) 4999–5003.

[14] M. Iwamatsu, Contact angle hysteresis of cylindrical drops on chemically heterogeneous striped surfaces, J. Colloid Interface Sci. 297 (2006) 772–777.

[15] D. Jacqmin, Calculation of two-phase Navier–Stokes flows using phase-field modelling, J. Comput. Phys. 155 (1999) 96–127.

[16] G. Karypis, V. Kumar, MeTis: unstructured graph partitioning and sparse matrix ordering system, version 4.0, http://www.cs.umn.edu/~metis, University of Minnesota, Minneapolis, MN, 2009.

[17] B.S. Kirk, J.W. Peterson, R.H. Stogner, G.F. Carey, libMesh: a C++ library for parallel adaptive mesh refinement/coarsening simulations, Eng. Comput. 22 (2006) 237–254.

[18] H. Kusumaatmaja, J.M. Yeomans, Modeling contact angle hysteresis on chemically patterned and superhydrophobic surfaces, Langmuir 23 (2007) 6019–6032.

[19] W. Li, A. Amirfazli, A thermodynamic approach for determining the contact angle hysteresis for superhydrophobic surfaces, J. Colloid Interface Sci. 292 (2005) 195–201.

[20] H.K. Moffatt, Viscous and resistive eddies near a sharp corner, J. Fluid Mech. 18 (1964) 1–18.
[21] N.A. Patankar, Transition between superhydrophobic states on rough surfaces, Langmuir 20 (2004) 7097–7102.
[22] T. Qian, X.-P. Wang, P. Sheng, Molecular scale contact line hydrodynamics of immiscible flows, Phys. Rev. E 68 (2003) 016306, pp. 1–15.
[23] W. Ren, Wetting transition on patterned surfaces: transition states and energy barriers, Langmuir 30 (2014) 2879–2885.
[24] A.J. Salgado, A diffuse interface fractional time-stepping technique for incompressible two-phase flows with moving contact, ESAIM: Math. Model. Numer. Anal. 47 (2013) 743–769.
[25] J. Shen, X. Yang, H. Yu, Efficient energy stable numerical schemes for a phase field moving contact line model, J. Comput. Phys. 284 (2015) 617–6305.
[26] D. Sivakumar, K. Katagiri, T. Sato, H. Nishiyama, Spreading behavior of an impacting drop on a structured rough surface, Phys. Fluids 17 (2005) 100608, pp. 1–10.
[27] X.-P. Wang, T. Qian, P. Sheng, Moving contact line on chemically patterned surfaces, J. Fluid Mech. 605 (2008) 59–788.
[28] X. Xu, X.-P. Wang, Derivation of the Wenzel and Cassie equations from a phase field model for two phase flow on rough surface, SIAM J. Appl. Math. 70 (2010) 2929–2941.
[29] X. Xu, X.-P. Wang, Analysis of wetting and contact angle hysteresis on chemically patterned surfaces, SIAM J. Appl. Math. 71 (2011) 1753–1779.
[30] P. Yue, C. Zhou, J.J. Feng, Spontaneous shrinkage of drops and mass conservation in phase-field simulations, J. Comput. Phys. 223 (2007) 1–9.